

High-Speed Imaging of Droplet Impact on a Hypervelocity Projectile

A. R. Dworzanczyk,^{*} and N. J. Parziale[†]
Stevens Institute of Technology, Hoboken, NJ 07030, USA.

N. J. Mueschke,[‡] D. J. Grosch[§] and P. Bueno[¶]
Southwest Research Institute, San Antonio, TX 78238, USA

The effects of liquid and solid impacts on aerospace bodies are of interest to hypersonics research. Collisions with precipitation or suspended dust particles can degrade aerospace materials, reducing transparency and other desirable properties. The bulk mechanical properties of a material are not always useful for estimating the effects of these interactions due to the small length scales involved, on the order of the material's own granularity or composite microstructure. At the same time, the interaction with the shock structure around a vehicle can disrupt a droplet, potentially altering the deleterious effects of impact. Since the sphericity and mass of an impacting drop both impact the degree of damage it does to relevant materials in a high-speed collision, it is important to characterize the exact breakup behavior of droplets in a multiphase flow system around an aerospace structure. Our approach is to use the Southwest Research Institute (SwRI) Light Gas Gun (LGG) facility to accelerate relevant materials to high velocities, introduce some prescribed form of precipitation, and study the multiphase flow interactions using advanced diagnostic techniques, namely direct shadowgraphy. A 5 MFps camera was used to image the interaction of a projectile at 2.4 km/s velocity with a stream of liquid water droplets in a low-pressure nitrogen medium. Two test shots were carried out in early 2022 to validate the structural integrity of the test projectiles and to test the imaging apparatus in conjunction with the SwRI LGG and liquid dropper mechanism. These preliminary results show that edge-stripping behavior, liquid jetting from the droplet-projectile impact point, and other multiphase hypersonic flow phenomena are present in the experiment. The liquid dropper mechanism, though successfully tested in the laboratory prior to installation at the LGG facility, proved less cooperative in the field setting, and is undergoing further refinement to assure consistent droplet quality in future experiments. The velocity of liquid jetting from collisions with the alumina projectile was measured and found to be between 1 and 2 times the collision velocity. Drop flattening was measured for small drops processed by an oblique shock.

I. Nomenclature

γ	=	surface tension
d	=	diameter
f	=	frequency
M	=	Mach Number
μ	=	Viscosity
Oh	=	Ohnesorge Number
R	=	Universal gas constant
r	=	radius
Re	=	Reynolds Number
ρ	=	Density

^{*}Graduate Student, Mechanical Engineering, 1 Castle Point on Hudson, Hoboken, New Jersey, 07030, USA.

[†]Associate Professor, Mechanical Engineering, 1 Castle Point on Hudson, Hoboken, New Jersey, 07030, Associate Fellow AIAA Member.

[‡]Program Manager, Southwest Research Institute, San Antonio, TX 78238.

[§]Senior Manager, Southwest Research Institute, San Antonio, TX 78238.

[¶]Lead Engineer, Southwest Research Institute, San Antonio, TX 78238.

σ_c	=	compressive yield stress of material
σ_t	=	tensile yield stress of material
$\sigma_{1,2,3}$	=	principal stresses in material
T	=	temperature
t	=	time
t_c	=	Characteristic Breakup Time
u	=	velocity
We	=	Weber Number

II. Introduction

THE effects of liquid and solid impacts on aerospace bodies are of interest to hypersonics research because of the potential for degradation of aerospace materials [1]. Collisions with precipitation or suspended dust particles can reduce transparency and other desirable properties [2]. The bulk mechanical properties of a material are not always useful for estimating the effects of these interactions due to the small length scales involved, on the order of the material's own granularity [3, 4]. At the same time, the interaction of the shock structure around a vehicle can disrupt a droplet, potentially altering the deleterious effects of impact [5–7]. Smaller liquid droplets can be destroyed entirely before impact by shock interactions. Since the sphericity and mass of an impacting drop both impact the degree of damage it does to relevant materials in a collision, it is important to characterize the exact breakup behavior of droplets in a multiphase flow system around an aerospace structure. Our approach is to use the Southwest Research Institute (SwRI) Light Gas Gun (LGG) facility to accelerate relevant materials to high velocities, introduce some prescribed form of precipitation, and study the multiphase flow interactions using advanced diagnostic techniques, namely direct shadowgraphy [8–11]. A 5 MFps camera was used to image the interaction of a projectile at 2.4 km/s velocity with a stream of liquid water droplets in N_2 at ≈ 175 torr. Two test shots were carried out in early 2022 to validate the structural integrity of the test projectiles and to test the imaging apparatus in conjunction with the SwRI LGG and liquid dropper mechanism. These preliminary results show that edge-stripping behavior, liquid jetting from the droplet-projectile impact point, and other multiphase hypersonic flow phenomena are present in the experiment. The liquid dropper mechanism, though successfully tested in the laboratory prior to installation at the LGG facility, proved less cooperative in the field setting, and is undergoing further refinement to assure consistent droplet quality in future experiments. Two further shots were carried out after modification to the liquid dropper mechanism.

III. Liquid Droplet Generator

Liquid droplets in the size range 0.1 to 4.0 mm are of interest to the United States Office of Naval Research (ONR) Multidisciplinary University Research Initiative (MURI). In order to generate consistently-sized spherical liquid droplets, the University of Maryland (UMD) designed a droplet generator driven by an acoustic shaker (or bass speaker). The liquid droplet generator works on the principle that a small surface disturbance on a liquid jet rapidly becomes amplified by the liquid's surface tension in a process of positive feedback until the jet snaps. A regularly-applied, small-magnitude disturbance can therefore break up a constant-velocity liquid jet into a stream of evenly-spaced, identically-sized droplets. This principle was documented in experimental and computational studies by [12], and the equation relating the optimal separation distance λ between consecutive droplets to the properties of the liquid jet is given by:

$$\lambda = \sqrt{2\pi d_0} \sqrt{1 + \frac{3\mu_0}{\sqrt{\rho_0 \gamma d_0}}} \quad (1)$$

Because of the incompressibility of liquids in the relevant range of pressures, the consequent droplet radius is related to the droplet spacing by:

$$(1/4)\lambda d_0^2 = (4/3)r_d^3 \quad (2)$$

A theoretical optimal frequency for the initial disturbing force applied to the liquid jet is given by:

$$f = u/\lambda \quad (3)$$

Density (kg/m ³)	Viscosity (kg/m s)	Surface Tension (N/m)
999	0.001	0.072

Table 1 Distilled Water Properties

Orifice Diameter (mm)	Drop spacing (mm)	d (mm)
0.5	2.239	0.943
1.0	4.444	1.882

Table 2 Calculated Droplet Sizes

The optimal frequency is a function of the diameter of the orifice from which the jet proceeds and the properties of the liquid. Table 1 gives the relevant properties for distilled water and Table (2) gives the calculated droplet spacing and diameter for orifices of diameter 0.5 mm and 1.0 mm.

The research presented here used a slightly-modified version of the UMD droplet generator design. Changes were made to mount the dripper to existing ports of ballistic-range testing at Southwest Research Institute (SwRI), including the need to provide an airtight seal between the droplet generator, the ballistic range, and the surrounding atmosphere, and to work within the physical confines of the SwRI ballistic range. A summary of the changes made to the UMD design is given:

- Outside diameter reduced from 7" to 4" because of available space in ballistic range window.
- Total number of brass orifice tubes reduced to 1.
- Number of fasteners drastically reduced due to smaller size of droplet generator.
- Second port added to water tank. This port was intended for use as a sight glass to check water level, but proved unnecessary since the tank is always full when the generator is in use.
- O-rings respecified for new generator dimensions.
- A two-piece external collar was devised in order to allow free rotation of the droplet generator in the ballistic range window. This allows precise control of the location of the generated droplet stream to ensure that droplets fall perpendicular to the axis of a projectile.

A side-by-side comparison of the two generator designs is given in Fig. 1

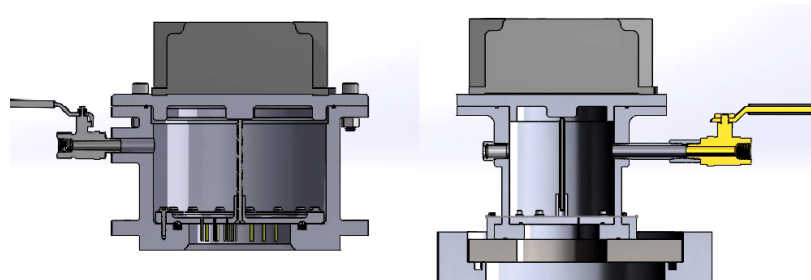


Fig. 1 UMD Droplet Generator design (left) and derived Stevens Droplet Generator design (right). Note smaller diameter and reduced number of brass tubes in Stevens design.

The modified droplet generator design was fabricated and tested at Stevens Institute of Technology. The bass speaker is controlled by a DS 345 function generator, which produces a signal that is fed into a JVC amplifier. A Nikon D3400 camera was used to image droplets at a 5 ms exposure time; the shadows of these droplets, projected against a white index card marked with a metric ruler, were used to determine the sphericity and diameter of the generated droplets.

Testing at Stevens Institute of Technology found that the optimal frequency for drop generation had very little relation to the theoretical optimal frequency given in Equation 3. The process of optimizing drop sphericity and spacing was in fact found to be a process of trial and error as various frequencies were attempted. The optimal frequency at which drops could be generated was also found to vary depending on the magnitude of the initial disturbance (that is, the volume of the signal supplied to the bass speaker), an unexpected complication to experimental setup. Nevertheless, in the laboratory setting, the drop generator was made to produce spherical, evenly-spaced drops of the expected diameter



Fig. 2 Shadows of 1.8 mm drops against index card with millimeter length scale, generated using first droplet generator design

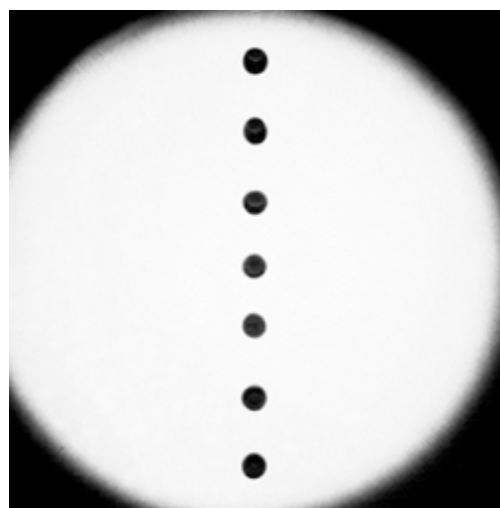


Fig. 3 0.9 mm drops backlit and imaged by Kirana high-speed camera, after droplet generator design revision

for orifices of 1 mm diameter. An image of the shadow cast by these drops against an index card is given in Fig. 2.

A. Drop Generator Refinement between Shots 2 and 3

Though the liquid droplet generator performed well in initial laboratory testing at Stevens Institute of Technology, it proved much more difficult to use in a satisfactory manner when attached to the ballistic range at SwRI. Combinations of frequency and amplitude that produced useful droplets at Stevens were less successful at SwRI. It was also noted that, at certain frequencies, the entire ballistic range began to vibrate, while shaking of the droplet generator's orifice plate and brass tubes, perceptible tactilely at Stevens, was no longer perceptible. It was suspected that the thickness and stiffness of the orifice plate was too great; thinner plates made of plastic were manufactured for testing.

Furthermore, it was desired to generate smaller droplets with a lower characteristic breakup time; the gravity-driven water feed system used during initial testing was sufficient to drive water through orifices of 1 mm diameter, but provided insufficient pressure for smaller tubes. Consequently, an electric pump was installed to increase the water pressure to generate smaller droplets.

The initial droplet generator design relied on transmitting vibration from the bass speaker to the brass tube through a threaded rod that attaches to the orifice plate and abuts the water tank lid, to which the speaker is attached with bolts. This required a painstaking process of assuring that the threaded rod was installed such that it pressed up against the lid, but not so much as to prevent the lid from tightly sealing against the tank. It also produced a weak transmission of

vibration to the center of the orifice plate. In order to correct this deficiency, the droplet generator was redesigned to attach the speaker directly to the orifice plate by means of a threaded rod. The bass speaker was dismantled to expose the center hole; the center hole was threaded and a new threaded rod was inserted. The opposite end of this rod threaded directly into the orifice plate, producing a rigid connection between the speaker and the orifice plate. To make the system watertight, an O-ring was fitted to a smooth part of the rod. The system is depicted in CAD imagery in Fig. 4.

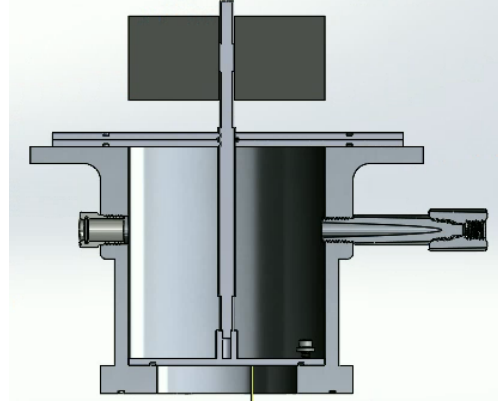


Fig. 4 Revised Drop Generator used for testing late in 2022, 2022

The revised droplet generator design was used to generate smaller (0.9 mm diameter) droplets in the laboratory at Stevens Institute of Technology. These drops were successfully generated, as shown in Fig. 3, which was taken at a distance of 12" below the exit from the brass tube. These backlit images were taken with the Kirana camera and use the same light source as was used at SwRI.

While attempting to study the process by which drops break off from the jet emanating from the brass tube, it was found that newly-generated droplets have a tendency to oscillate between a spherical shape and a more flat shape. Fig. 5 demonstrates this phenomenon; among seven consecutive drops, the first and last are seen to be fully spherical, while those in between grow more and then less flat. This phenomenon suggests that the process of droplet formation, which relies on surface tension amplifying small disturbances to the surface of a water jet, leaves new drops with residual mechanical energy that gradually damps out as the drop falls (hence the more uniform shape of the droplets farther away from the brass tube). It was not noted by Shimasaki and Taniguchi [12], but this might result from the use of a much heavier liquid in that experiment. Further research to test this hypothesis would require analyzing the characteristics of liquid drops with different properties.

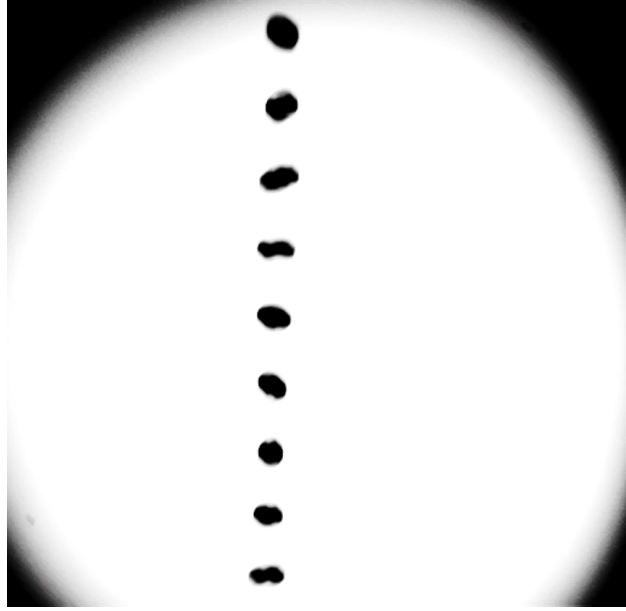


Fig. 5 Drops oscillating from spherical to flattened and back.

IV. Projectile Design and Fabrication

Slender projectiles were designed and fabricated for ballistic range experiments in 2021 [9]. These experiments revealed that, for brittle materials of interest (alumina and carbon-carbon composite), the slender projectile design produced unacceptably high stress concentrations that led to projectile failure in flight. Furthermore, the slender projectile bodies had been mounted in a discarding sabot to fit the SwRI LGG bore. Incomplete sabot separation compromised test results even when more durable projectiles survived launch. The projectiles were redesigned in order to mitigate or eliminate stress concentrations and sabot-separation event and ensure the possibility of studying projectile interaction with liquid droplets.

Instead of a long, slender body made from the brittle materials of interest, small, spherical cap sections were fabricated and attached to a polycarbonate bore rider. This bore rider, unlike the sabots used before, remains attached to the projectile tip for the full duration of the experiment. In order to move the center of mass forward and ensure stability in flight, a projectile holder was manufactured from tungsten-copper alloy. This projectile holder threads into the polycarbonate bore rider, and the projectile tip is adhered to it with a high-strength epoxy (Ablestik 2151).

Prior to fabrication, finite-element analysis simulations of the stresses and strains within the projectiles were executed to increase confidence in material survivability. An explicit dynamics simulation was carried out in ANSYS of a fully-assembled projectile with a fully-dense alumina tip. Southwest Research Institute supplied three acceleration vs. time curves for 0.25 kg projectiles. The acceleration curves for 0.25 kg projectiles supplied by Southwest Research Institute is supplied in Fig. 6. The 1D hydrocode prediction for gun performance overpredicts gun muzzle velocity for a given propellant load by $\approx 10\%$. To compensate for this tendency, SwRI includes a knockdown factor of 10% to 12%—that is, the code optimizes the propellant load for a muzzle velocity 88% to 90% as great as the desired velocity. The acceleration profile calculated for a 12% knockdown factor, therefore, represents the most aggressive launch profile, and this profile is the one used in the explicit dynamics simulations. The acceleration profile is converted into a time-varying pressure boundary condition on the aft face of the full bore rider projectile in the ANSYS explicit dynamics simulation by multiplying the acceleration by the projectile mass and dividing by the cross-sectional area. A zero radial displacement boundary condition is applied to the outer surface of the polycarbonate projectile base because, in practice, the steel gun barrel would prevent radial deformation. Fig. 7 illustrates the applied boundary conditions for the explicit dynamics simulation.

The chosen acceleration profile shows a maximum expected acceleration of almost $7E5 \text{ m/s}^2$. When the average acceleration of the simulated projectile reaches or exceeds this value, the simulation is stopped and stresses on the projectile components are reported. Since the acceleration at the step at which stresses are reported will actually exceed $7E5 \text{ m/s}^2$, by $\approx 20\%$, the reported stress values calculated by ANSYS are considered conservative.

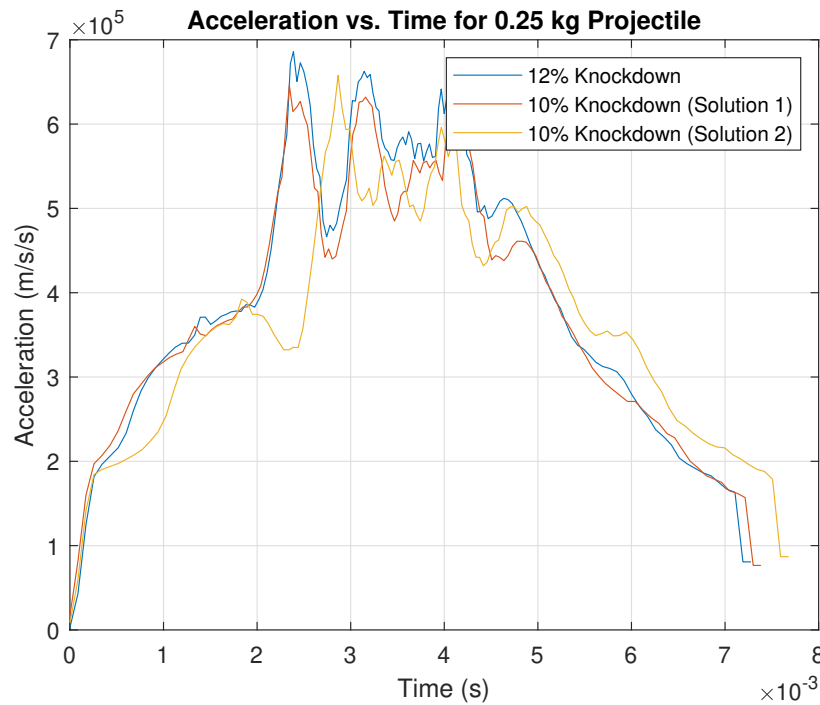


Fig. 6 Acceleration vs. Time Curves supplied by SwRI

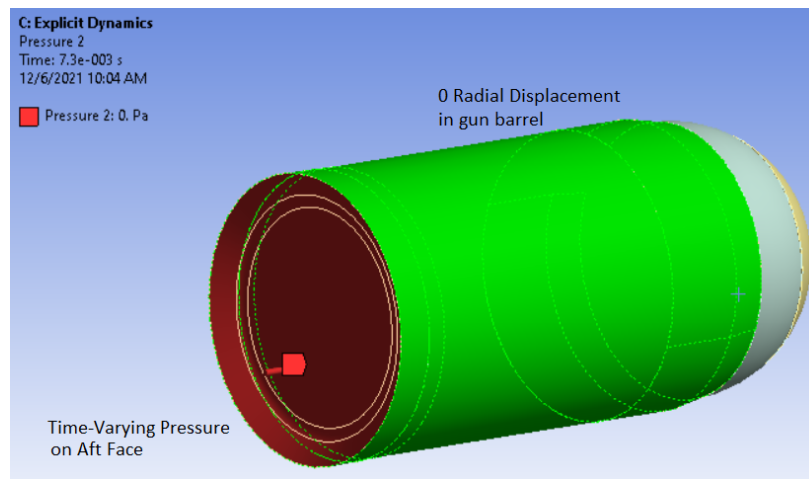


Fig. 7 Simulation Boundary Conditions

The simulated projectile tip and tip holder are meshed with an unstructured grid with a body sizing of 2 mm. The polycarbonate base also uses an unstructured grid with 2 mm body sizing, except near where the tungsten-copper projectile holder contacts it. In this region, a mapped mesh with a 0.5 mm edge sizing is used. The total number of elements is 188,525, and the mesh is depicted in Fig. 8.

Fig. 9 gives the stress distribution on the flat, aft face of the fully-dense alumina projectile tip at peak acceleration. The compressive stress here reaches a maximum value of 165 MPa. This is far below (by a safety factor of 14) the yield stress of fully dense alumina in compression (2.6 GPa). The maximum stress is reached in an annular region on the aft face of the tip. No stress concentration was observed in the simulation results. Fig. 10 shows the safety factor distribution for this component.

Fig. 11 gives the stress distribution in a section view along the middle of the tungsten-copper projectile tip holder. The maximum stress in this component is 464 MPa. This stress is reached in the filleted region immediately forward

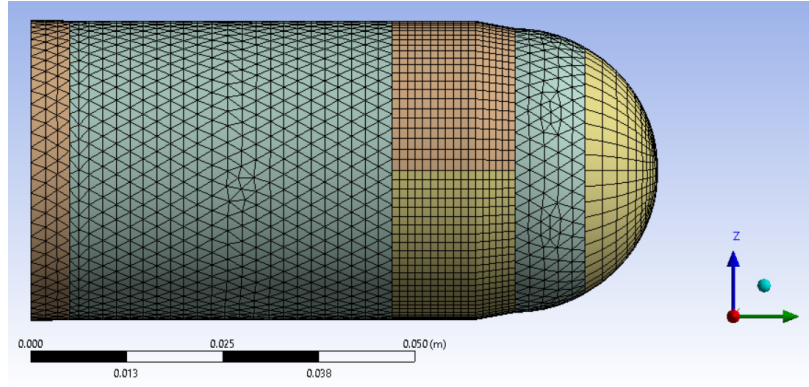


Fig. 8 Mesh used in Projectile Explicit Dynamics Simulation

of the holder's threads. This is an expected stress concentration location. The yield stress of the tungsten-copper alloy is 585 MPa, so a safety factor of 1.26 is maintained even in this conservative analysis. Fig. 12 shows the safety factor distribution in the tungsten-copper tip holder.

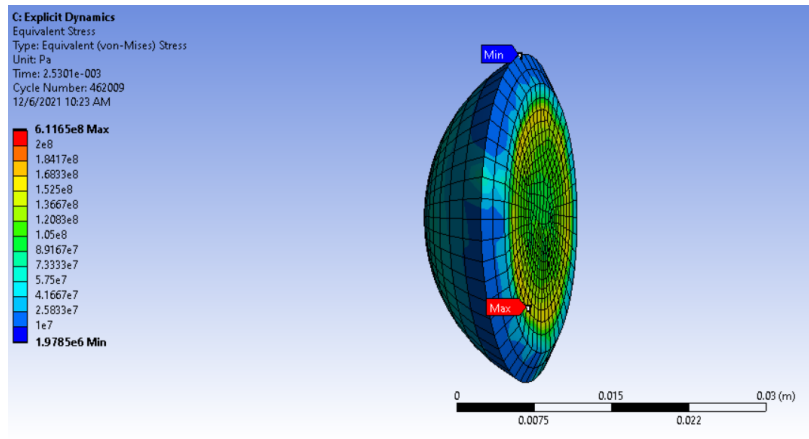


Fig. 9 Stress in Fully Dense Alumina Projectile Tip

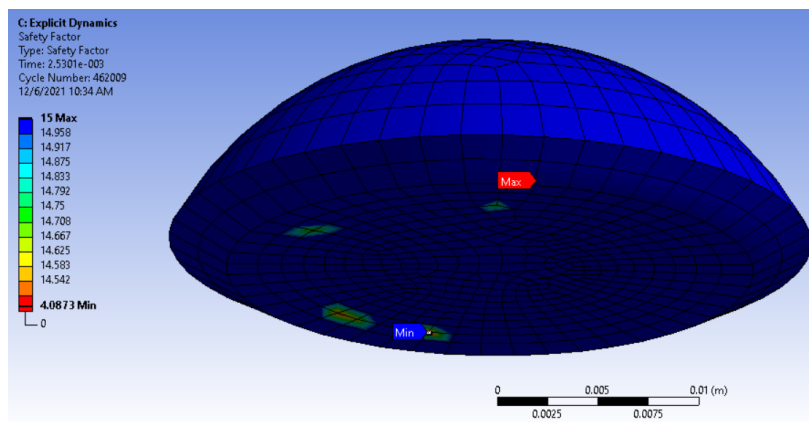


Fig. 10 Safety Factor in Fully Dense Alumina Projectile Tip

The maximum principle stresses in the alumina tip were also compared to the Christensen failure criterion for

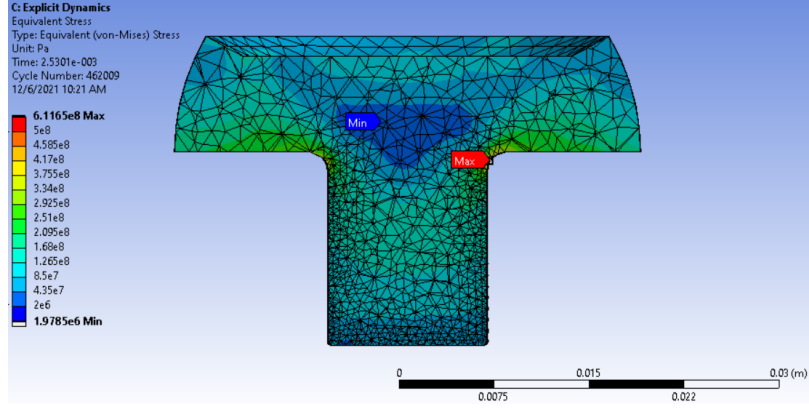


Fig. 11 Stress in Tungsten-Copper Projectile Tip Holder

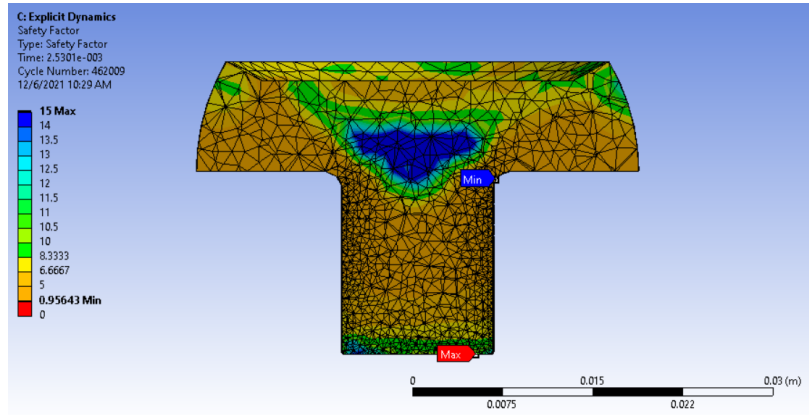


Fig. 12 Safety Factor in Tungsten-Copper Projectile Tip Holder

fully-dense alumina. The Christensen failure criterion [13] relates the principle stresses in an isotropic material to the material's tensile and compressive yield stresses:

$$\left(\frac{1}{\sigma_t} - \frac{1}{\sigma_c}\right)(\sigma_{xx} + \sigma_{yy} + \sigma_{zz}) + \frac{1}{\sigma_t \sigma_c} \left\{ \frac{1}{2} [(\sigma_{xx} - \sigma_{yy})^2 + (\sigma_{yy} - \sigma_{zz})^2 + (\sigma_{zz} - \sigma_{xx})^2] \right\} \leq 1 \quad (4)$$

In terms of principle stresses, Eq. 4 can be rewritten as:

$$\left(\frac{1}{\sigma_t} - \frac{1}{\sigma_c}\right)(\sigma_1 + \sigma_2 + \sigma_3) + \frac{1}{\sigma_t \sigma_c} \left\{ \frac{1}{2} [(\sigma_1 - \sigma_2)^2 + (\sigma_2 - \sigma_3)^2 + (\sigma_3 - \sigma_1)^2] \right\} \leq 1. \quad (5)$$

Alumina's tensile yield stress is one tenth of its compressive yield stress, so it is a brittle material. This imposes an additional failure criterion, that the maximum principle stress must be less than the tensile yield stress:

$$\text{Max}(\sigma_1, \sigma_2, \sigma_3) \leq \sigma_t \quad (6)$$

Solving Eq. 5 with the simulated values for principle stress, it is found that the left side of the equation adds up to 0.57, which is safely less than 1. Eq. 6 is satisfied as well, since the maximum principle stress in the alumina tip is only 85 MPa, which is \approx three times less than the tensile yield stress of alumina.

Based on the successful execution of explicit dynamics simulations of an accelerating projectile, it was concluded that mechanical failure of the projectile during launch will be unlikely. High confidence was achieved that the full-bore-rider, spherical-tipped projectile will avoid the sabot separation and stress wave concentration issues that troubled the earlier, slender projectiles. Parts were ordered and fabricated immediately thereafter. A photograph of four assembled projectiles, with tips of alumina and carbon-carbon, is given by Fig. 13.

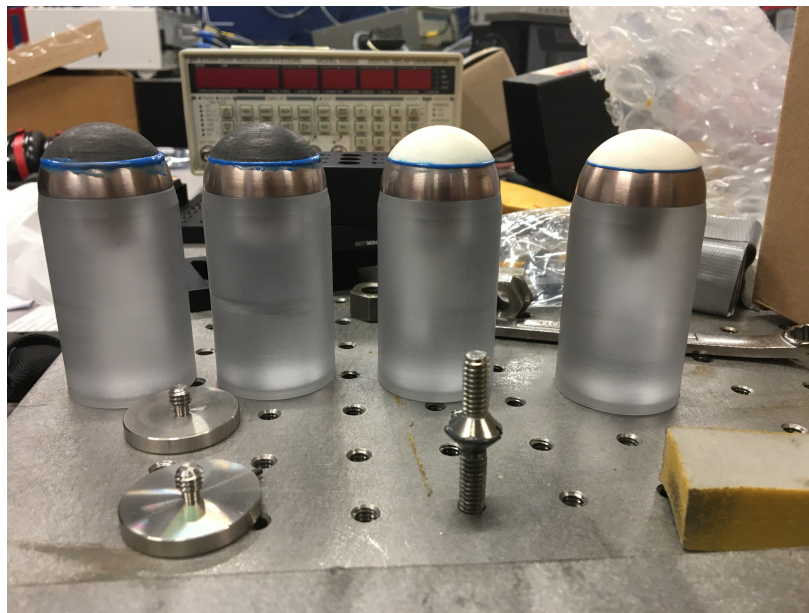


Fig. 13 Assembled projectiles with carbon-carbon (left two) and alumina (right two) tips.

V. Experimental Setup

The SwRI LGG facility is a multistage gas gun capable of accelerating projectiles to over 6,000 m/s [14]. It is depicted in Fig. 14. For these experiments, a velocity of 2.5 km/s was targeted. The acceleration required to reach this velocity is up to $7E5$ m/s/s, or $\approx 71,000$ G.



Fig. 14 Southwest Research Institute Light Gas Gun

Downrange of the gas gun muzzle, the projectile passes through a blast tank, with an X-ray apparatus emplaced 66" downrange to image the projectile. X-ray images of the projectile after leaving the gun muzzle allow confirmation that the projectile survived launch and a control image against which to study the impacts of multiphase interaction. Imaging the projectile at a second X-ray station 144" from the muzzle allows precise calculation of the actual launch velocity.

A Kirana high-speed camera recording at 5 million frames per second is mounted so as to point through an

optically-clear window at a stream of droplets introduced into the test environment by the droplet generator described in Sec. III. The camera's field of view measures 2.07" wide by 1.71" tall. Illumination is provided by a Cavilux laser. A laser trigger is used to start the recording; when the beam is interrupted by the projectile, the Cavilux laser delivers a 36 microsecond pulse of light. This light is collimated by a parabolic mirror on the opposite side of the ballistic range from the Kirana camera and reflected toward the camera. The Kirana camera records 180 frames at 5 Mfps.

18" downrange from the Kirana camera, a Phantom TMX 7510 camera is used for backlit shadowgraph imaging of the projectile after droplet interaction. A laser light source is also used for this camera. Like the Cavilux laser used for the Kirana camera, this laser is collimated using a parabolic mirror mounted on the opposite side of the ballistic range.

A flash X-ray imaging apparatus is placed at the next optical window downrange from the shadowgraph imaging setup, a further 18" downrange. Fig. 15 illustrates the placement of cameras, lasers, collimation mirrors, and X-ray equipment during the experiments.

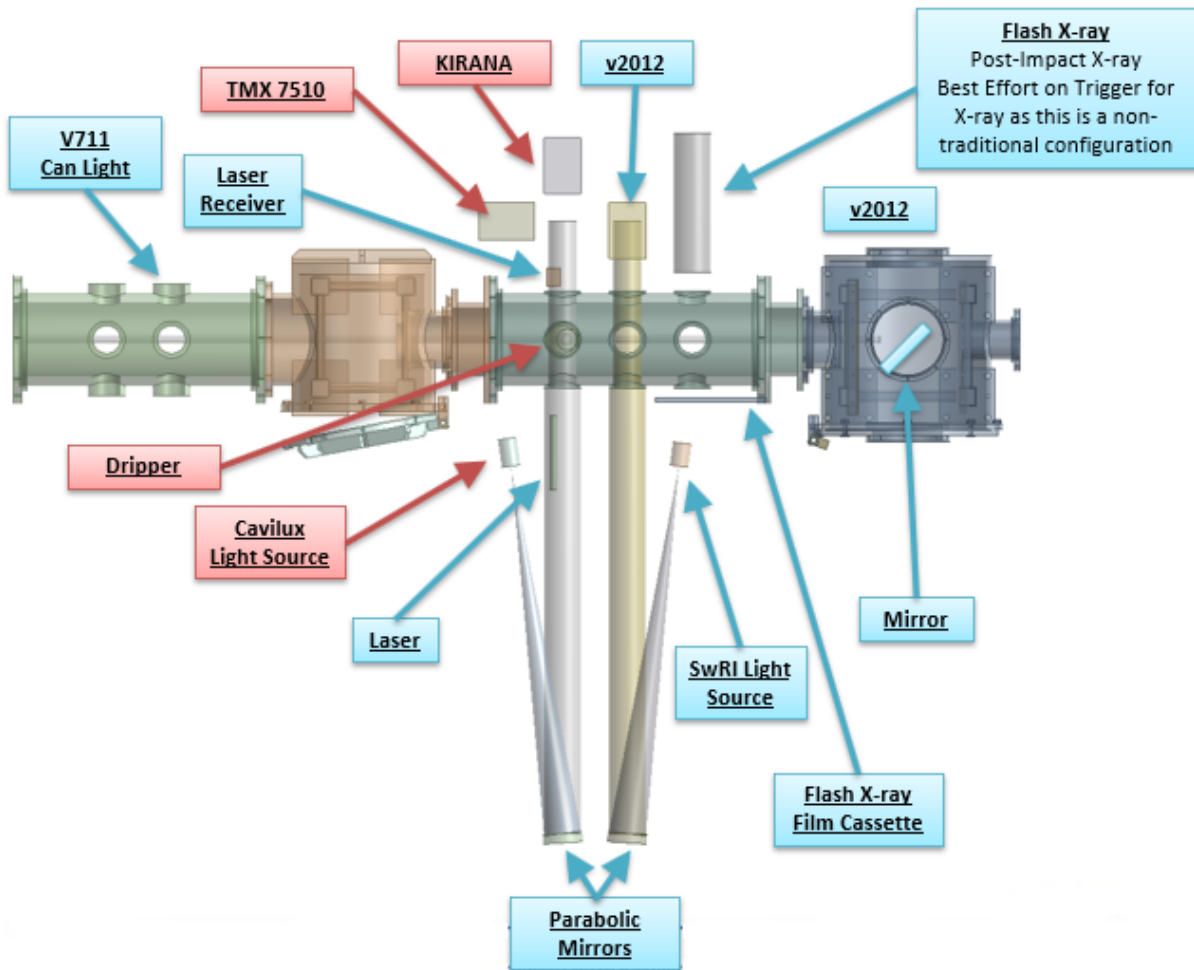


Fig. 15 Illumination and Imaging setup during ballistic range tests at SwRI

VI. Ballistic Range Testing

Here, we will present the results from two of the four shots that were conducted. The first shot used a full-bore-rider projectile with a fully-dense alumina projectile tip. The second shot used a full-bore-rider projectile with a 2.5D carbon-carbon composite tip. The first shot achieved a launch velocity of 2400 m/s into a pressure of 153 torr and a temperature of 295 K, while the second achieved a launch velocity of 2595 m/s into a pressure of 225 torr and a temperature of 295 K. X-ray and shadowgraph images were successfully generated for each shot.

Following repairs to the LGG, a further two test shots were carried out at SwRI, both using alumina tips. These shots, respectively reached velocities of 2430 and 2450 m/s, were fired into pressures of 154 and 160 torr and temperatures of 295 K. The corresponding Mach numbers were ≈ 7 for each shot. X-ray and shadowgraph images were generated for each shot. Issues with camera overexposure rendered the results of shot 3 unusable. For shot 4, the projectile yawed in flight away from the ballistic range centerline. Modifications to the drop generator between shots 2 and 3 included replacement of the 1 mm orifice used in the first two shots with a 0.5 mm orifice, resulting in a smaller expected drop diameter.

To parametrize the changes in droplet effects, the Weber, Ohnesorge, Reynolds, and Mach numbers for each shot are calculated. A characteristic drop breakup time t_c was also found in the literature [15] and calculated for the expected drop diameter for each shot. The equations for each non-dimensional parameter and characteristic time are given by:

$$\text{Ma} = u_p / \sqrt{\gamma RT} \quad (7)$$

$$\text{We} = \rho_g u_{\text{projectile}}^2 d / \sigma \quad (8)$$

$$\text{Oh} = \mu_d / \sqrt{\rho_d d \sigma} \quad (9)$$

$$\text{Re} = \sqrt{\text{We}} / \text{Oh} \quad (10)$$

$$t_c = \frac{d}{u_{\text{projectile}}} \sqrt{\frac{\rho_d}{\rho_g}} \quad (11)$$

The Mach, Ohnesorge, Weber, and Reynolds numbers, and the characteristic time for each shot, are tabulated in Tab. 3 for post-shock gas properties. The nominal drop diameter, shock standoff distance, and interaction duration (that is, the time for the projectile to cross the shock standoff distance) are also tabulated.

Shot	1 (Alumina)	2 (Carbon-Carbon)	3 (Alumina)	4 (Alumina)
Velocity (m/s)	2400	2595	2430	2450
Pressure (torr)	153	225	154	160
Nominal Diameter (mm)	1.8	1.8	0.9	0.9
Shock Standoff Distance (mm)[16]	2.58	2.58	2.58	2.58
Interaction Duration (μs)	1.08	0.99	1.06	1.05
Mach	6.94	7.41	6.94	7.00
Weber	163,000	283,000	79,000	84,000
Ohnesorge	2.4E-3	2.4E-3	3.5E-3	3.5E-3
Reynolds	167,000	220,000	80,000	83,000
Characteristic time (μs)	24.1	18.0	11.3	11.0

Table 3 Dimensionless Values and Characteristic Time for each shot

A. Shot 1: Fully-Dense Alumina

The first images generated during the fully-dense alumina shot are X-ray images of the projectile upon exiting the gun muzzle. As expected, the tungsten-copper projectile holder is most clearly visible due to its high density and metallic composition. The alumina projectile tip is also visible, with no apparent cracks or dislocation. The polycarbonate bore rider is more faint, but still clearly visible. No part of the projectile sustained damage during the launch, as can be seen in Fig. 16.

High-speed video recorded by the Kirana camera at 5 Mfps indicates that the projectile remains intact when it reaches the stream of droplets descending from the droplet generator. At the location dropper, the projectile is flying at a ≈ 5 -degree angle of attack. In addition to the large drops of ≈ 1.9 mm diameter expected, the droplet generator has

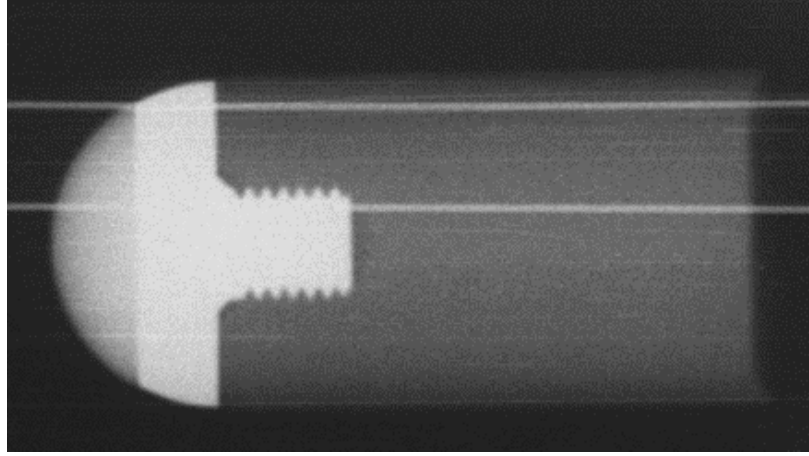


Fig. 16 Post-launch X-ray image of alumina-tipped projectile

produced a smaller number of much smaller (0.5-mm diameter) droplets along approximately the same line. A detached bow shock is visible in the high-speed video 2.3 mm ahead of the projectile tip. This bow shock first begins interacting with liquid droplets at frame 47, 9.4 microseconds after the camera is triggered. Between that time and frame 52, 1 microsecond later, bow shocks form around the liquid droplets nearest to the projectile tip. However, the droplets are so large and the interaction so fast that no apparent edge-stripping or other droplet breakup behavior seen in previous studies is observed during this period before the first droplet impacts the projectile tip. Fig. 17 shows the formation of the bow shocks around the droplets first encountered by the projectile.

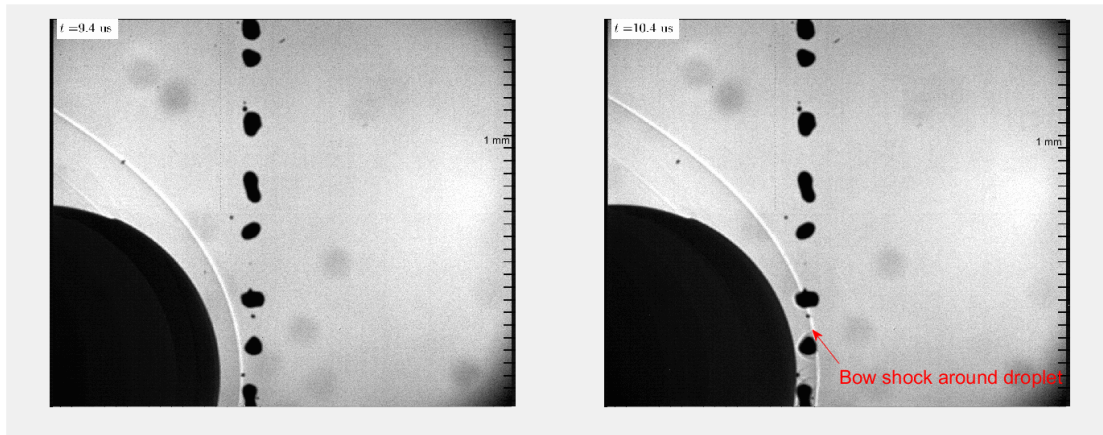


Fig. 17 First interaction of alumina-tipped projectile with droplet stream

Droplet-projectile interaction begins at frame 53, when a small drop (diameter ≈ 0.46 mm) and a large drop (diameter ≈ 1.71 mm) impact the center of the alumina projectile tip. Neither drop has been substantially changed in size or shape by aerodynamic forces before this point. During their impact, liquid water is seen jetting radially from the perimeter of the contact between the alumina and the water drops. Similar jetting behavior is observed as the projectile impacts other droplets in the field of view. The projectile traverses the diameter of a droplet in only one microsecond; this is an order of magnitude less than the characteristic breakup time of a droplet under these conditions ($\approx 20 \mu s$), so the lack of change to them before impact is consistent with previous literature. Fig. 18 indicates the location of the first projectile-droplet collision and the formation of a radial jet of water.

By tracking the advance of a liquid jet between consecutive frames, an estimate of the jet velocity can be made. Fig. 19 shows the beginning of jet propagation from one projectile-drop collision and its propagation between two

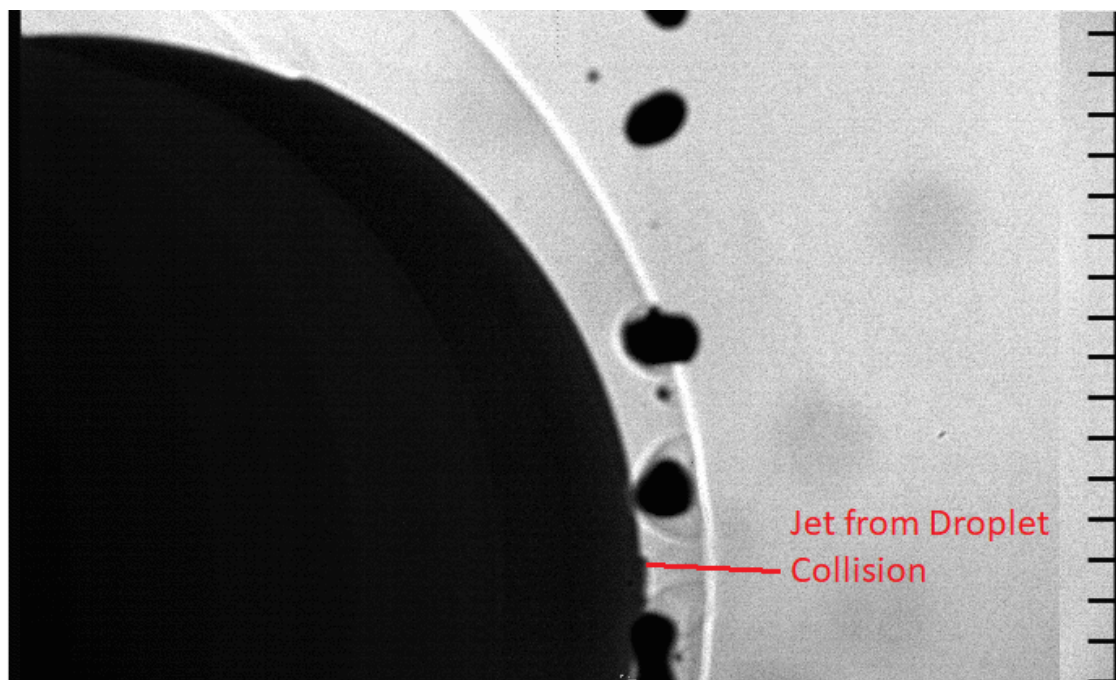


Fig. 18 Radial jet from first alumina projectile-droplet collision

consecutive frames. Prior literature indicates that the velocity of a jet emanating radially from a drop impact is between 2 and 5 times the impact velocity [17]. However, this estimate was made for the earliest part of an interaction between an incoming jet of liquid and a solid surface; its applicability to jetting from a discrete drop of liquid over a longer period is uncertain. A MATLAB script was written to track the progress of liquid water jets along a propagation vector. Four drops were found in the video to have clear jetting away from the point of collision. Propagation vectors were marked for each. Fig. 20 gives the four drops analyzed for this shot and the jet propagation vectors for each, marked against a binary, color-reversed frame from the backlit video. The calculated position (in mm from the starting point) as a function of time for jets from each of the four drops is illustrated in Fig. 21.

The four jets begin propagating from their respective origins at different times. Once the jets begin propagating, they continue along their initial propagation vector at roughly a constant speed. The slope of the curves in Fig. 21 gives the jetting velocity; in this shot, jet velocities range from 2.86 to 3.76 km/s. For each of the four drops that produced impact jetting, the jetting velocity is less than 2 times the velocity of the projectile (2.43 km/s). The jet from drop 4, farthest from the drop's center, slows slightly more than 1 μ s after that drop is struck. Jets from the other three drops are not observed more than 1 μ s after they originate because, in the other cases, these jets intersect neighboring drops or jets by that time. It is possible that this phenomenon would affect other drops if there was no interference from their neighbors. Fig. 21 appears to show jet "stalling" for drops 1 and 3; this is a numerical artefact of interaction with neighboring drops.

B. Shot 2: 2.5D Carbon-Carbon

The 2.5D carbon-carbon projectile tip did not survive launch intact. The first X-ray image of the projectile after launch shows a large gap between the carbon-carbon projectile tip and the tungsten-copper projectile holder to which it was adhered. Two lines of the same transparency as the carbon-carbon tip are visible in the space behind the tip; their similar brightness to the tip indicates that they are sheets of carbon-carbon material. There appears also to be a strand of carbon-carbon between the tip and one of these sheets. The X-ray image suggests that the carbon-carbon has delaminated. A failure of the Ablestik adhesive cannot be ruled out due to the high X-ray absorption of the tungsten-copper projectile holder. Fig. 22 shows the separation of the carbon-carbon projectile tip from the tungsten-copper projectile holder after launch, and the apparent sheets of carbon material behind the tip.

A later X-ray image, Fig. 23 and the high-speed imagery collected by the Kirana camera, show that the carbon-carbon tip has recontacted the tungsten-copper holder. The carbon-carbon tip is in off-center contact with the tungsten-copper holder when it passes through the stream of droplets. As a consequence of the carbon-carbon tip's structural failure, the

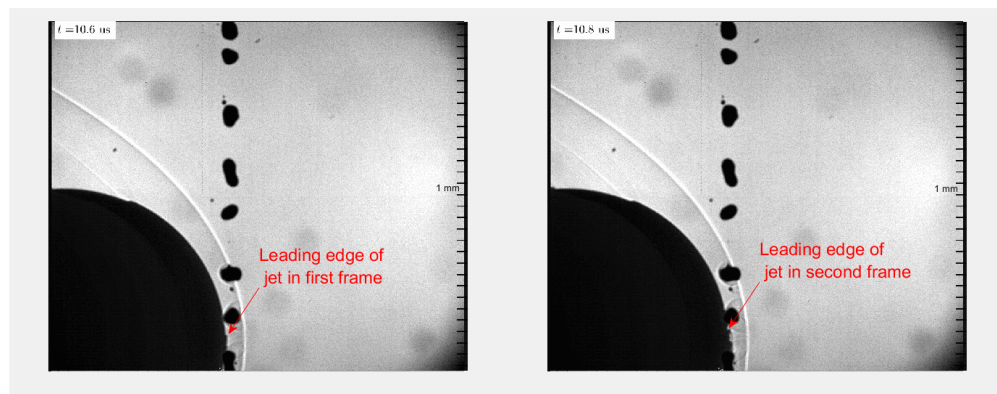


Fig. 19 Movement of radial jet over 0.2 μ s.

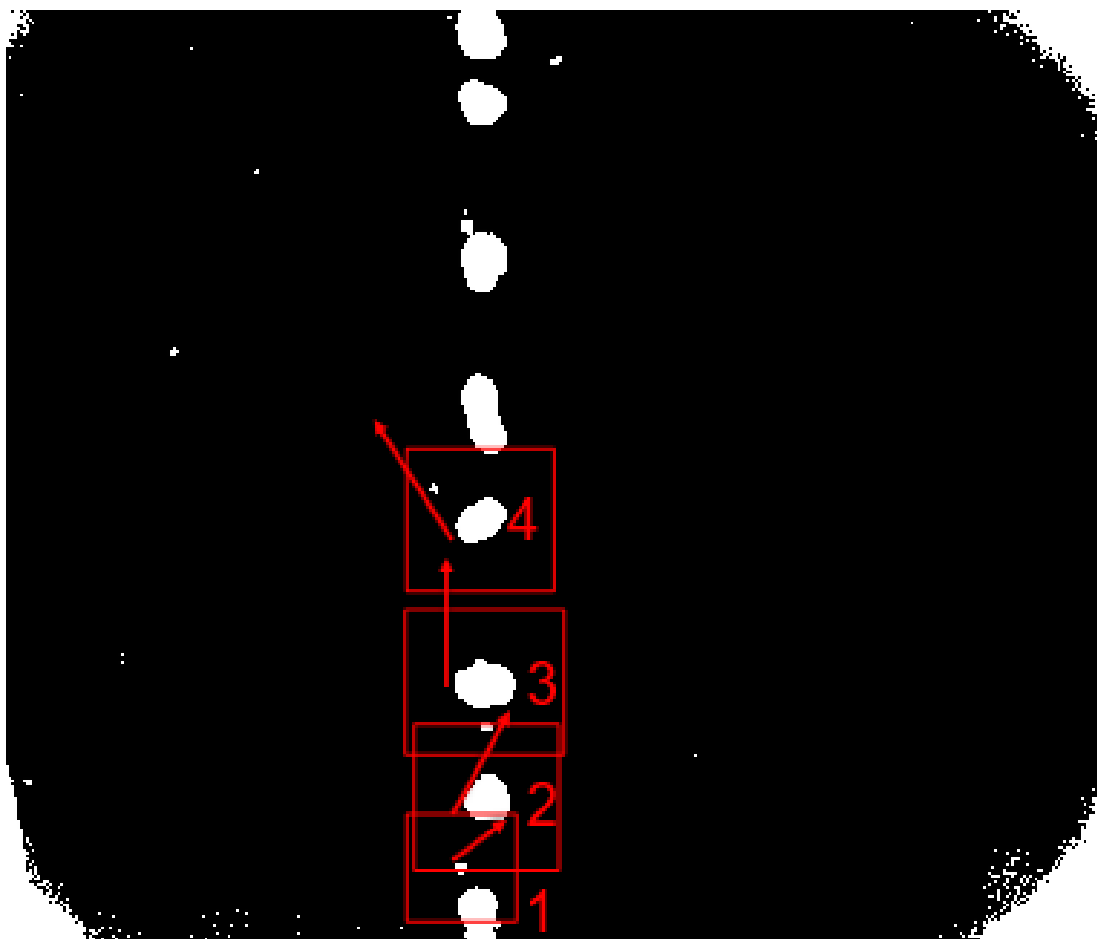


Fig. 20 Vectors of impact jet propagation in Shot 1

projectile is accompanied for the remainder of its flight by a cloud of carbon-carbon debris fragments.

As in the previous shot, the droplet generator produces a stream of drops less regular than those seen in laboratory testing at Stevens Institute of Technology. The drop diameters range from 0.3 mm to 2.0 mm. The Kirana camera is better-focused on the droplets during this test than the previous shot, but inherent features of the Kirana camera design

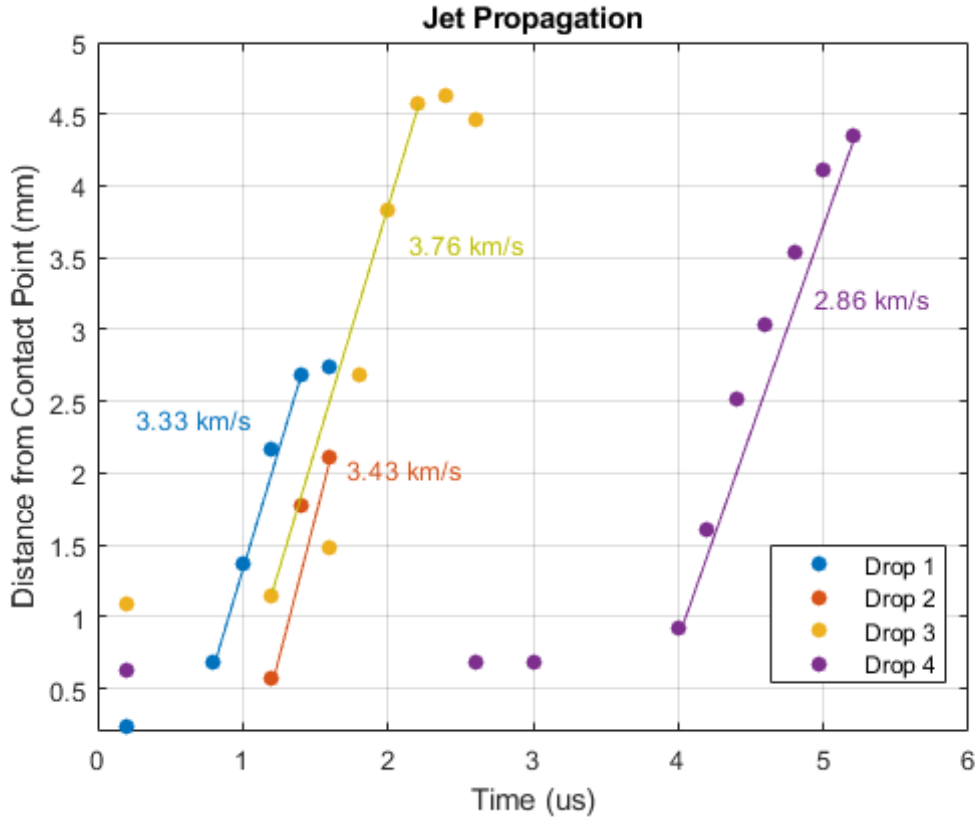


Fig. 21 Velocities of four jets identified in backlit video of Shot 1

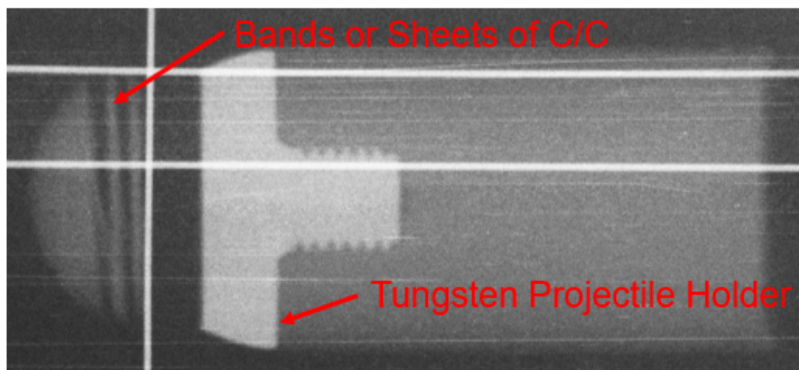


Fig. 22 Post-launch X-ray image of carbon-carbon-tipped projectile

produce dimmer duplicates ("ghosting") of the shadows of the projectile and its accompanying bow shock. Because of the detachment of the carbon-carbon projectile tip from the rest of the projectile, the droplet stream is not aligned with the center of the projectile tip; though the projectile tip first begins obscuring a droplet at frame 32, no evidence of liquid jetting from that drop is visible until frame 36, as shown in Fig. 24. Drops of interest for analysis are marked with letters A-H in this figure. The off-center collision makes it more difficult to estimate jet velocity by inspecting the position of the jet in subsequent frames, and made it impossible to check radial jet thickness. However, this was attempted anyway using the same technique described for the previous shot. The results, for labeled drops E, F, G, and H, are given in Fig. 25. For drops E and F, only two consecutive frames could be found for an approximation of jet velocity before the jet began interfering with a neighboring jet. For drop G, only three such frames were available. Drop

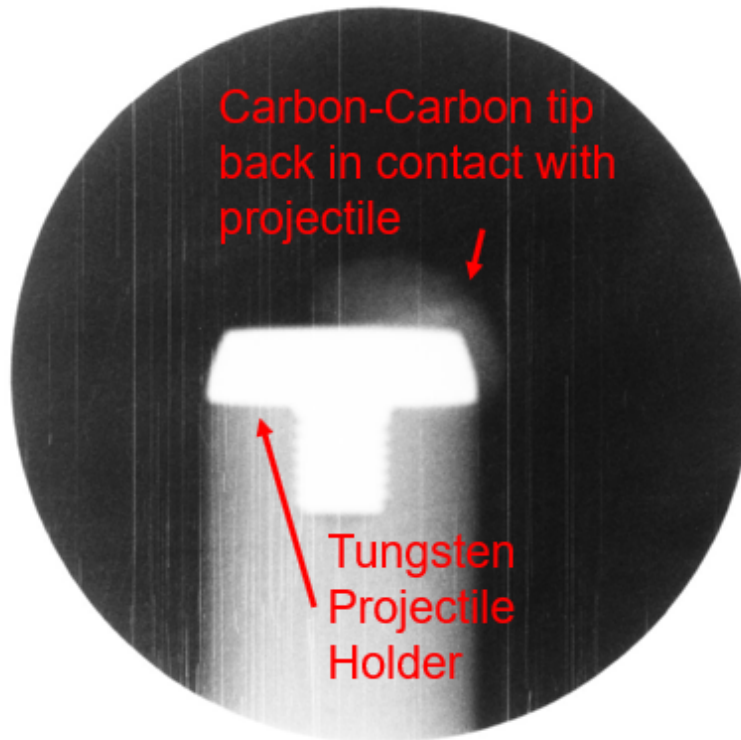


Fig. 23 X-ray image of carbon-carbon-tipped projectile captured further downrange, showing that the tip has recontacted the tungsten-copper projectile holder, albeit off-center

H had six consecutive frames over which the jet could be tracked. Consequently, the jetting velocities computed for this shot must be considered more approximate than those in the previous shot. The jetting velocity in this shot appears to be between 3.29 m/s and 4.46 km/s. As in the previous shot, this is less than twice the projectile's own velocity.

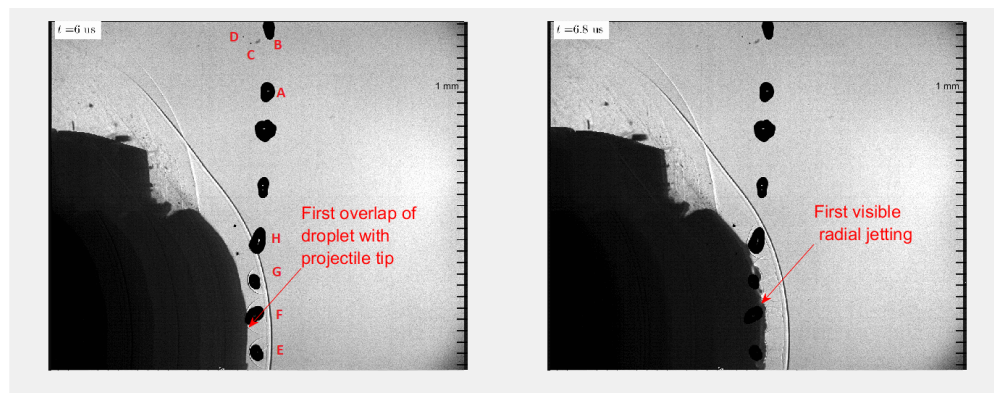


Fig. 24 First collision of carbon-tipped projectile with droplet.

As in the shot with the alumina projectile tip, the water droplets are seen to develop their own bow shocks after the projectile bow shock passes over them. Bow shocks can also be seen around the leading edges of the water jets expanding away from droplet-projectile collisions, as highlighted in Fig. 26.

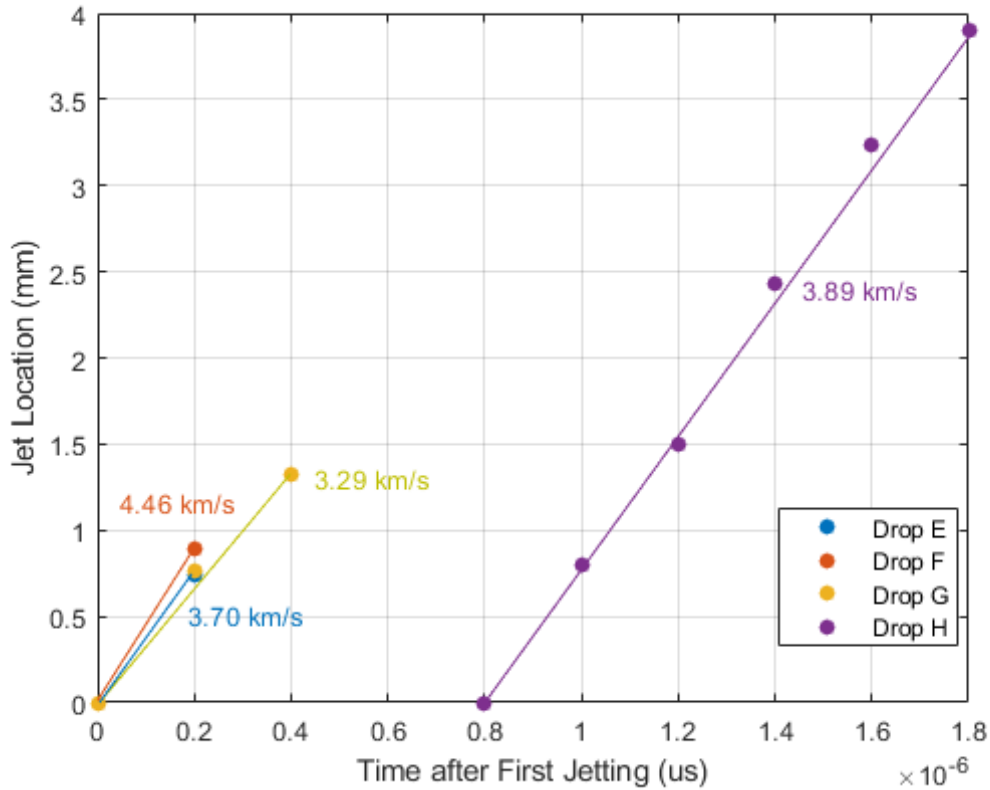


Fig. 25 Jet positions vs. time for four drops impacted by the 2.5D carbon-carbon projectile tip.

1. Drop Flattening and Breakup

While the droplets closest to the tip of the projectile do not survive long enough to experience the droplet breakup phenomena documented by previous researchers [5] [18], four droplets near the edge of the field of view are not impacted by the projectile, and can be seen to undergo similar breakup phenomena. Two of the droplets, marked A and B in Fig. 27 are large (diameter ≈ 1.8 mm), and experience edge-stripping behavior. That is, material is seen to be shed from the outer edges of the drops until they are obscured from view by the expanding cloud of debris from other droplets. The other two droplets, marked C and D, are much smaller (diameter ≈ 0.14 mm). These drops are seen to experience both flattening and edge-stripping behavior, and are propelled away from their initial position before the expanding debris plume blocks them from view. The calculated characteristic breakup time for these drops must be recalculated both because of their small diameter and because their off-axis position relative to the projectile's bow shock changes the expected post-shock air density. Approximating the local conditions by a conical shock of equal shock angle (48°), the post-shock density should be 1.561 kg/m^3 , while the post-shock gas velocity should be $\approx 1200 \text{ m/s}$. The calculated characteristic breakup time for droplets of this diameter in these conditions is $\approx 3 \mu\text{s}$. It is possible to calculate the non-dimensional diameter (that is, the diameter divided by the initial diameter) of these small drops as a function of non-dimensional time (time elapsed divided by characteristic breakup time) after first shock interaction, as was done by Hebert et al. [19]. For drops C and D, this is done in Fig. 28.

For both drops, a substantial duration of time (2-3 times the calculated characteristic breakup time) is available during which droplet evolution can be studied. Drop C increases in diameter until $\approx 1.25 T_c$, reaching a maximum diameter of 3 times its initial diameter around frame 78 of the video. After this point, the drop is seen to shed a quantity of material from its edges, and become narrower. The non-dimensional diameter decreases to less than 2.4 at time $1.5 T_c$. Drop D behaves similarly, increasing to 3 times its initial diameter before a large quantity of material is stripped off. The remaining drop after that stripping is narrower than Drop C, only 1.3 times its initial diameter. Both drops experience stripping when they reach a diameter three times their initial diameter, as shown in Fig. 29. Drop C experiences stripping around time $1.33 T_c$, while drop D experiences stripping around time $1.73 T_c$. These times

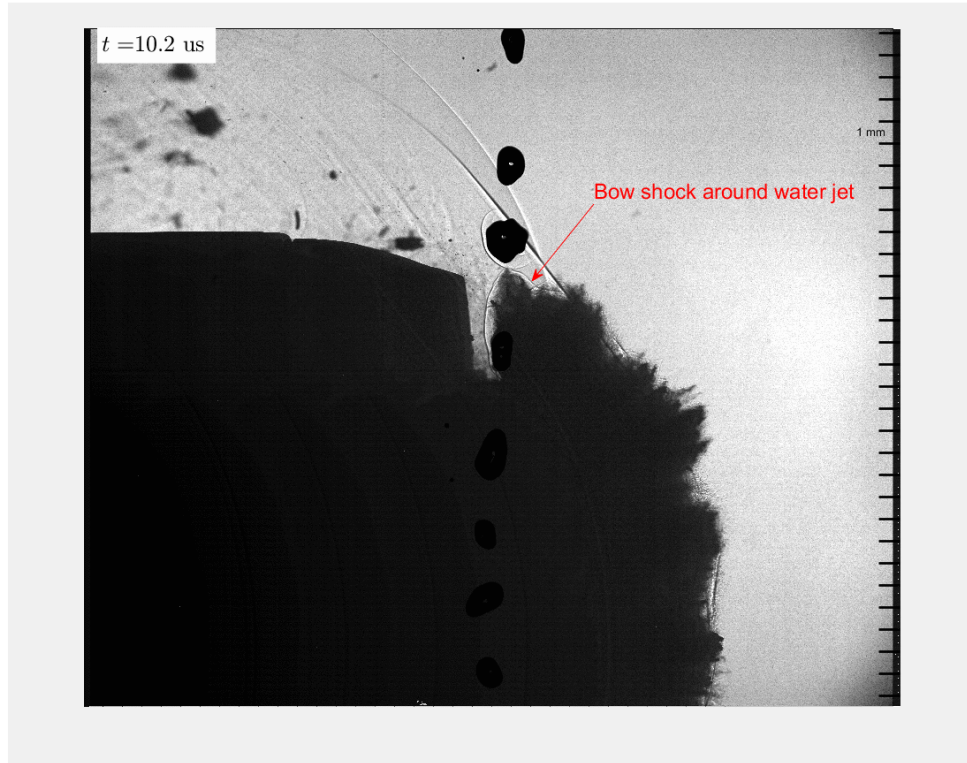


Fig. 26 Bow shocks around droplets and radial water jets

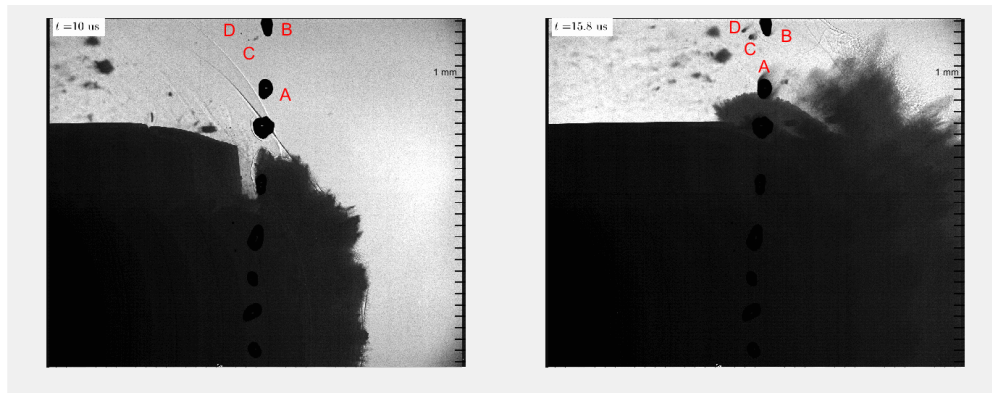


Fig. 27 Edge Stripping and Breakup of drops farther from projectile tip.

are consistent with the times of stripping observed by Hebert et al. [19], who also observed that the stripping takes place when the non-dimensional diameter reaches a value of ≈ 3 -3.5. Further study is required to determine whether a non-dimensional diameter of 3 constitutes some critical point at which mass stripping becomes more likely, and what physical mechanisms drive the phenomenon if so. Both drops become obscured by liquid jetting material from the other drops in the experiment and are not clearly visible after frame 100.

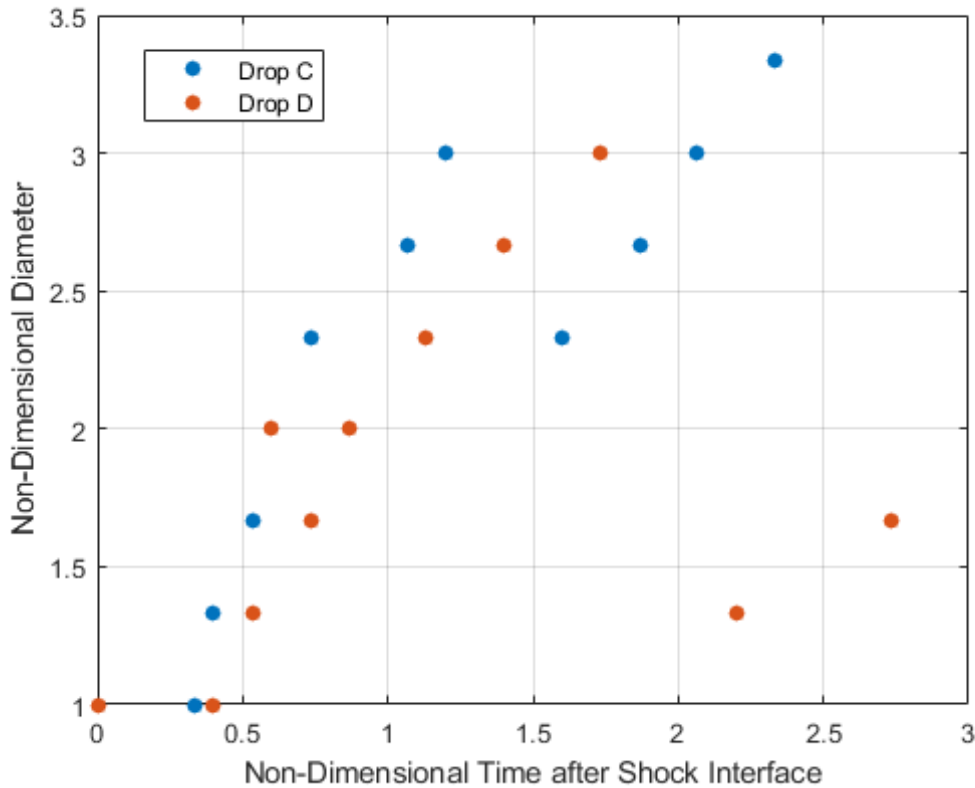


Fig. 28 Non-Dimensional Diameter vs. Non-Dimensional Time for Drops C and D in Shot 2

C. Shot 3: Alumina

The third shot was conducted on after repairs to the LGG were conducted, and after the liquid drop generator was modified to use a 0.5 mm orifice rather than a 1.0 mm orifice. Theoretically, that should have yielded drops of diameter 0.9 mm. The projectile successfully impacted a stream of liquid water droplets. Unfortunately, an error made during camera set-up resulted in oversaturated video data. While "splashing" of water from the projectile-drop collisions can be observed in the recorded video, it is unclear which splash corresponds to which drop. The shock structures around the projectile are also totally washed out, and no evolution in drop shape can be observed in those not directly impacted by the projectile.

D. Shot 4: Alumina

As with shot 3, an alumina-tipped projectile was used for Shot 4. This time, the camera was correctly configured to record the projectile-drop interactions, but the projectile itself appears to have yawed considerably away from the range centerline. Figure 30 gives an X-ray image of the projectile from this shot. In addition to a substantial pitch away from the horizontal plane (almost 10 degrees), the projectile shows a substantial yaw, as demonstrated by the tungsten-copper ballast occluding part of both the alumina tip and the polycarbonate bore rider in the image.

A consequence of the projectile's yaw in this shot is that the collision between the projectile and the drop is not visible in the backlit shadowgraph imagery. The rounded tip of the projectile itself occludes that collision, and with it the first stages of jetting away from the drops in this shot. While the jetting splash from the drops becomes visible several frames after the impact takes place, the origin of the jets cannot be determined with certainty, and the velocity component of the jets toward or away from the camera makes it difficult to determine the precise jetting velocity.

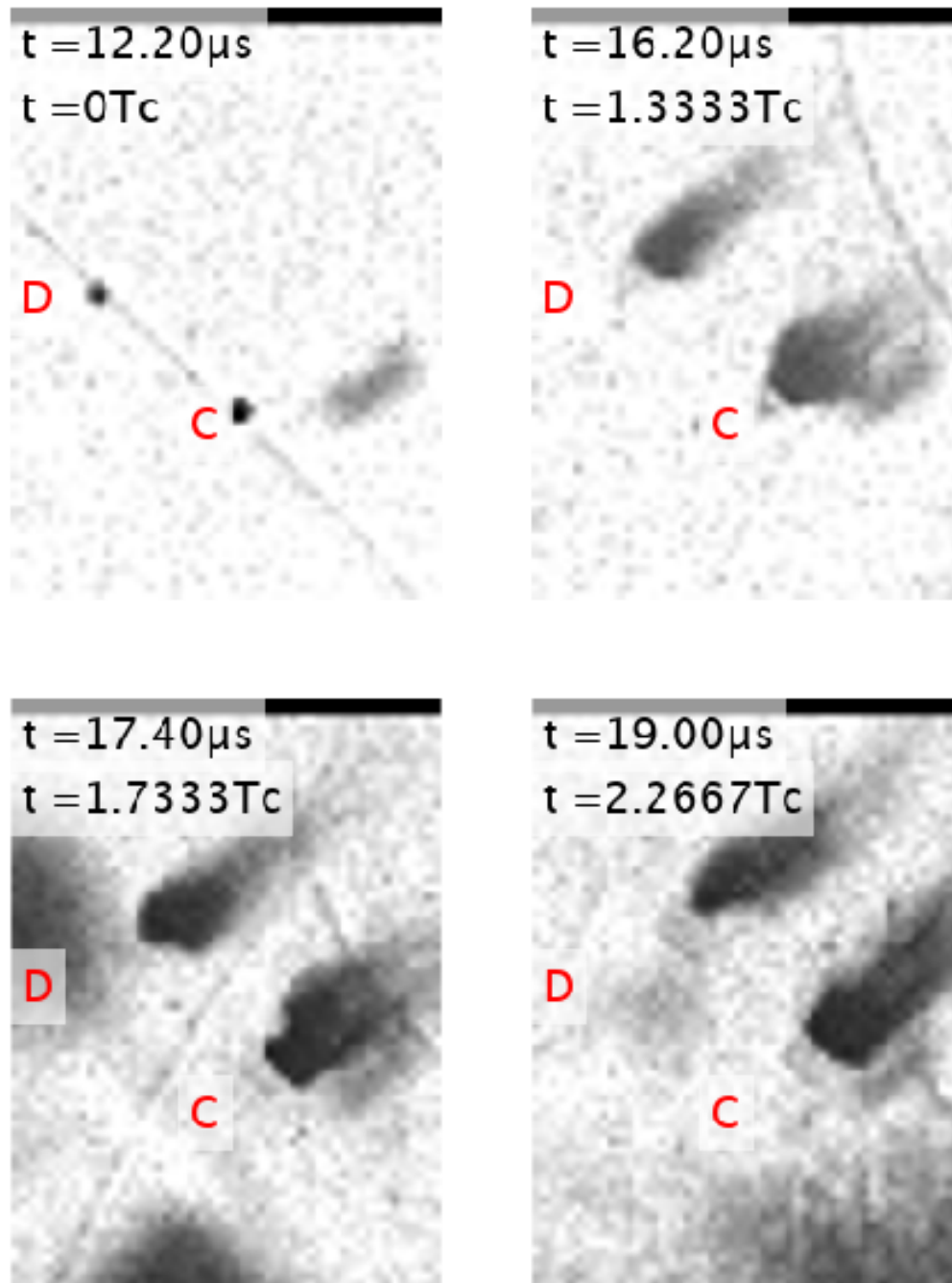


Fig. 29 Stripping of Material from Drops C and D in Shot 2

VII. Future Work

While projectiles have been fabricated and successfully launched to hypersonic velocities, the inconsistent quality of liquid droplets remains a major concern. It is suspected that the use of a large collector tank in the original drop generator design poses problems with the regulation of flow velocity; since the tank is full of water, it provides a source

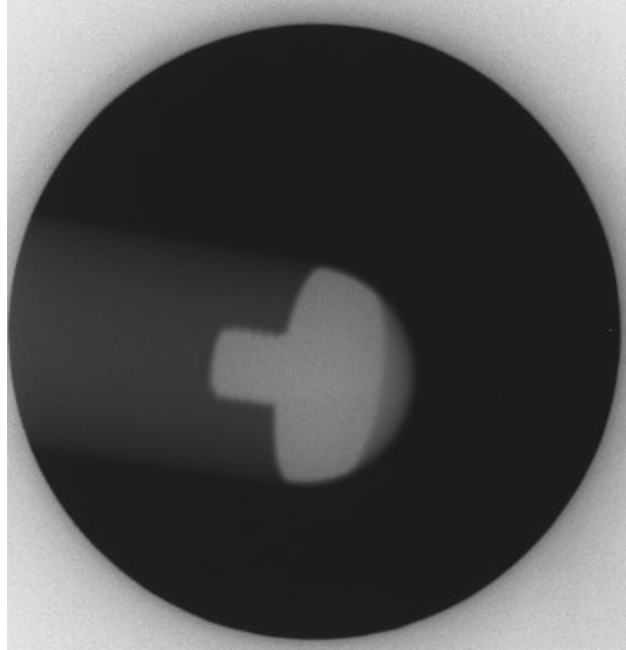


Fig. 30 X-Ray image of Shot 4 projectile, showing severe pitch and yaw

of hysteresis in the overall flow system, and makes it unresponsive to attempts to change flow velocity. Since a very precise combination of disturbance frequency and flow velocity is required to generate even, spherical drops, the current effort to improve the drop generator centers on eliminating the tank. Instead, the nozzle in the newest design runs directly through the speaker that provides the disturbance force. The current drop generator is depicted in Fig. 31.



Fig. 31 Drop Generator modified to eliminate collection tank

VIII. Conclusions

In support of the objectives of the Office of Naval Research (ONR) Multidisciplinary University Research Initiative (MURI), experiments were carried out to study the interaction of hypersonic bodies with liquid droplets simulating weather phenomena. A liquid drop generator was built and tested. High-speed imaging techniques involving synchronized pulsed lasers were used to produce shadowgraph images of collisions between hypersonic projectiles and liquid droplets. A new projectile design was analyzed using finite element analysis and found to survive launch when the tip was made of fully-dense alumina. Droplet breakup phenomena were observed similar to those described in previous research. Drop impact jetting and drop flattening were quantified, and the change of drop non-dimensional diameter was plotted against non-dimensional time. Drop impact jetting velocity was found to be considerably less than was expected from literature values analyzing jetting velocities early in a collision process. Drop flattening behavior was found to match that in previous literature, and investigation is ongoing to determine the nature of the physical processes that drive flattening and stripping. Further refinement of the droplet generation and imaging processes is ongoing.

Acknowledgements

Dworzanczyk and Parziale were supported by ONR-MURI Grant N00014-20-1-2682. The research would not have been possible without the support of Nicholas Mueschke, Donald Grosch, and Pablo Bueno at Southwest Research Institute, nor would it have been possible without the use of that facility's Light Gas Gun. **Special thanks** go out to Mr. Ben Seagall of Stevens Institute of Technology for his assistance in executing the finite element analysis portion of this work, and to Mr. Paul McClelland and Mr. Bruce Fraser of the Stevens Institute of Technology machine shop.

References

- [1] Moylan, B., Landrum, B., and Russell, G., "Investigation of the Physical Phenomena Associated with Rain Impacts on Supersonic and Hypersonic Flight Vehicles," *Procedia Engineering*, Vol. 58, 2013, pp. 223–231. <https://doi.org/10.1016/j.proeng.2013.05.026>.
- [2] Lapp, R. R., Stutzman, R. H., and Wahl, N. E., "A Study of Rain Erosion in Plastics and Metals," WADC 53-185, 1954.
- [3] Adler, W. F., "Investigation of Liquid Drop Impacts on Ceramics," ETI-CR-82-1075, 1982.
- [4] Adler, W. F., "Rain impact retrospective and vision for the future," *Wear*, Vol. 233-235, 1999, pp. 25–38.
- [5] Reinecke, W. G., and McKay, W. L., "Experiments on Water Drop Breakup Behind Mach 3 to 12 Shocks," SC-CR-70-6063, 1969.
- [6] Barber, J. P., Taylor, H. R., Grood, E. S., and Hopkins, A. K., "Water Drop/Bow Shock Interactions," AFML-TR-75-105, 1975.
- [7] Barber, J. P., "Water Drop Breakup/Impact Damage Thresholds," AFML-TR-76-126, 1976.
- [8] Danehy, P. M., Weisberger, J., Johansen, C., Reese, D., Fahringer, T., Parziale, N. J., Dedic, C., Estevadeordal, J., and Cruden, B. A., "Non-Intrusive Measurement Techniques for Flow Characterization of Hypersonic Wind Tunnels," *Flow Characterization and Modeling of Hypersonic Wind Tunnels (NATO Science and Technology Organization Lecture Series STO-AVT 325)*, NF1676L-31725 - Von Karman Institute, Brussels, Belgium, 2018.
- [9] Dworzanczyk, A., and Parziale, N. J., "High-Speed, Short-Pulse-Duration Light Source for Digital Inline Holographic Imaging of Multiphase Flow Fields," *Proceedings of AIAA Aviation Forum 2021*, AIAA-2021-2919, Virtual Event, 2021. <https://doi.org/10.2514/6.2021-2919>.
- [10] Dworzanczyk, A., Parziale, N. J., Mueschke, N. J., Grosch, D. J., and Bueno, P., "Material Survivability on Launch of Slender Ballistic Range Projectiles," *Proceedings of AIAA Scitech 2022*, AIAA-2022-0772, San Diego, California and Virtual Event, 2022. <https://doi.org/10.2514/6.2022-0772>.
- [11] Dworzanczyk, A., and Parziale, N. J., "High Speed Diagnostics for the Study of Droplet Breakup," *Proceedings of the 20th International Symposium on Application of Laser and Imaging Techniques to Fluid Mechanics*, Lisbon Symposia, Lisbon, Portugal, 2022.
- [12] Shimasaki, S., and Taniguchi, S., "Formation of uniformly sized metal droplets from a capillary jet by electromagnetic force," *Applied Mathematical Modeling*, Vol. 35, 2011, pp. 1571–1580.

- [13] Christensen, R. M., “A Comprehensive Theory of Yielding and Failure for Isotropic Materials,” *J. Eng. Mater. Technol.*, Vol. 129(2), 2007, pp. 173–181. <https://doi.org/10.1115/1.2712847>.
- [14] Mueschke, N. J., Walker, J. D., and Grosch, D., “Examination of Atmospheric Density Scaling Effects on Sub-Scale Hypersonic Flight Bodies Using a Ballistic Launch Facility,” *Proceedings of the 23rd AIAA International Space Planes and Hypersonic Systems and Technologies Conference*, AIAA-2020-2444, Montreal, Quebec, Canada, 2020. <https://doi.org/10.2514/6.2020-2444>.
- [15] Reinecke, W. G., and Waldman, G. D., “A Study of Drop Breakup Behind Strong Shocks with Applications to Flight,” AVSD-0110-70-RR, 1970.
- [16] Liepmann, H. W., and Roshko, A., *Elements of Gasdynamics*, John Wiley and Sons, Inc., 1957.
- [17] Engel, O. G., “Waterdrop collisions with solid surfaces,” *Journal of Research of the National Bureau of Standards*, Vol. 54, No. 5, 1955, p. 281. <https://doi.org/10.6028/JRES.054.033>.
- [18] Wierzbna, A., and Takayama, K., “Experimental Investigation of the Aerodynamic Breakup of Liquid Drops,” *AIAA Journal*, Vol. 26, No. 11, 1988, pp. 1329–1335.
- [19] Hebert, D., Rullier, J., Chevalier, J., Bertron, I., Lescoute, E., Viot, F., and El-Rabii, H., “Investigation of mechanisms leading to water drop breakup at Mach 4.4 and Weber numbers above 10^5 ,” *SN Applied Sciences*, Vol. 2, 2020. <https://doi.org/10.1007/s42452-019-1843-z>.